

Domain Generalization of 3D Object Detection by Density-Resampling

Shuangzhi Li, Lei Ma, and Xingyu Li

Department of Electrical and Computer Engineering, University of Alberta, Alberta, Canada

{shuangzh, lma7, xingyu}@ualberta.ca

Abstract

Point-cloud-based 3D object detection suffers from performance degradation when encountering data with novel domain gaps. To tackle it, the single-domain generalization (SDG) aims to generalize the detection model trained in a limited single source domain to perform robustly on unexplored domains. In this paper, we propose an SDG method to improve the generalizability of 3D object detection to unseen target domains. Unlike prior SDG works for 3D object detection solely focusing on data augmentation, our work introduces a novel data augmentation method and contributes a new multi-task learning strategy in the methodology. Specifically, from the perspective of data augmentation, we design a universal physical-aware density-based data augmentation (PDDA) method to mitigate the performance loss stemming from diverse point densities. From the learning methodology viewpoint, we develop a multi-task learning for 3D object detection: during source training, besides the main standard detection task, we leverage an auxiliary self-supervised 3D scene restoration task to enhance the comprehension of the encoder on background and foreground details for better recognition and detection of objects. Furthermore, based on the auxiliary self-supervised task, we propose the first test-time adaptation method for domain generalization of 3D object detection, which efficiently adjusts the encoder’s parameters to adapt to unseen target domains during testing time, to further bridge domain gaps. Extensive cross-dataset experiments covering “Car”, “Pedestrian”, and “Cyclist” detections, demonstrate our method outperforms state-of-the-art SDG methods and even overpass unsupervised domain adaptation methods under some circumstances. The code will be made publicly available.

1. Introduction

LiDAR-based 3D object detection is a crucial task in real-world applications, such as autonomous driving [1, 30] and UAV sensing [13, 51]. Deep learning-based models [1, 30, 31, 47, 51] are the mainstream for 3D object de-

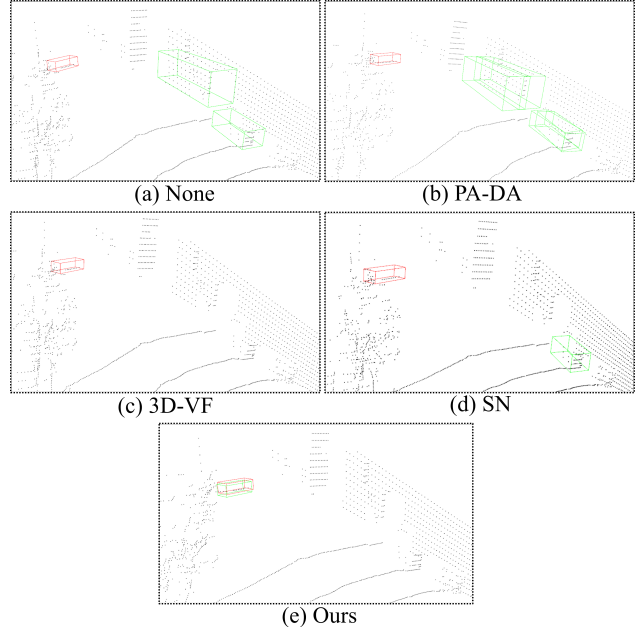


Figure 1. Detection results w.r.t. Waymo → NuScenes, where the red boxes are ground-truth 3D boxes and green ones are detected 3D boxes. Our method achieves better performance than other SDG methods, PA-DA [8] and 3D-VF [19], and even UDA method SN [42] (refers to Table 2 for statistical details).

tection. However, when these models encounter data with domain gaps (e.g., adverse weather [11, 12, 17], diverse laser scanning densities [15], and shifted object sizes [42]), their performance declines significantly. To tackle it, unsupervised domain adaptation (UDA) [15, 42, 49] focuses on adapting the model to a new domain distribution during training with the help of unlabeled target data. Targeting a more general case, domain generalization (DG) [16, 27, 39] endeavors to enhance the model’s generalizability with no access to target data during model training.

The approaches of domain generalization in 3D object detection can be primarily categorized into multi-domain generalization and single-domain generalization. Multi-domain generalization (MDG) [35, 45] utilizes diverse

source domain knowledge to bridge the unseen target domain gaps. Given the high diversity of real-world domains, 3D data collection and label annotation for multiple source domains is costly. In this paper, we focus on the more universal yet more challenging single-domain generalization (SDG) setting, where the model learns from a single source domain only. The primary challenge of SDG lies in how to rely on limited single-domain information to enable a model to achieve domain-invariant learning and therefore perform robustly on diverse unseen domains. Though single-domain generalization [54] has gathered significant attention in various 2D image tasks (e.g., classification [43], detection [38], and segmentation [28]), it's still under-explored in the context of the 3D point cloud, especially for object detection. Prior works in SDG of 3D object detection like *PA-DA* [8] and *3D-VF* [19] usually utilize data augmentation to synthesize more 3D data, aiming to eliminate domain-dependent information in model learning. Yet, no effort has been reported from the learning methodology perspective.

In this work, we tackle the SDG problem from both data augmentation perspective and multi-task learning strategy. The former bridges the domain gap mainly introduced by various point densities, and the latter facilitates representation learning through 3D scene restoration and test-time adaptation. Specifically, our data physical-aware data augmentation stems from our observation in intra-domain 3D object detection: *the low point density is highly correlated to object miss-detection*. As demonstrated in Figure 2, object occlusion [46] causes significant local point density reduction and various distances between objects and the laser sensor [14] also cause variations in the point density on imaged objects. In inter-domain cases, further considering adverse weather (e.g., rain [17], snow [12], and fog [11]) that may cause the reduced intensity of reflected light resulting in sparse laser scans and the diverse 3D sensors with different scanning beam layers, we hypothesize that the issue introduced by point density variations becomes more pronounced in inter-domain object detection. In this regard, we design a universal physical-aware density-resampling data augmentation (PDDA) to mitigate the performance loss stemming from diverse point densities. Unlike prior augmentation methods for domain generalization of 3D object detection like *PA-DA* [8] and *3D-VF* [19] that modify point density augmentation in a localized and random manner, our PDDA re-samples the point clouds following real-world imaging physical constraints, thus better accounting for different density patterns.

From the learning methodology viewpoint, we propose a multi-task learning for point-cloud-based 3D object detection. Specifically, during source training, besides the standard detection task, we design an auxiliary self-supervised task to restore the globally uniformly masked points by density downsampling. Recently, some research [3, 53] has

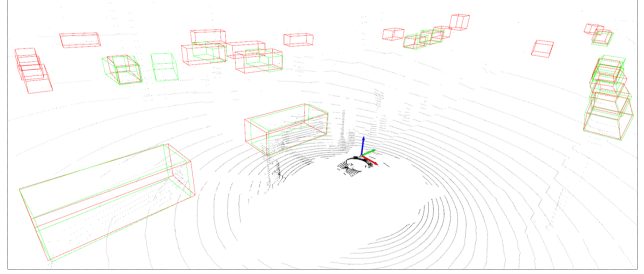


Figure 2. Intra-domain detection by VoxelRCNN [9] with voxel-based backbone on NuScenes. Due to the blockage by front objects and various distances, cars with sparse scanning are hard to detect. (red boxes are ground-truth 3D boxes and green ones are detected 3D boxes)

shown that background information is also crucial in object recognition and detection. By working with the standard detection task, our self-supervised task helps the encoder to better comprehend the background and foreground details in point clouds, which benefits the recognition and detection of objects. Furthermore, during the testing time, leveraging the auxiliary self-supervised task for 3D scene restoration, we design the restoration loss to measure the quality of restoration on the target domain data. Based on the loss, we efficiently adjust the encoder's parameters with lightweight optimization to adapt the encoder to unseen target domain shifts, thereby further bridging domain gaps. In summary, this work makes the following contributions:

- To tackle the erroneous object detections caused by diverse point densities, we design a straightforward yet effective universal physical-aware density-resampling data augmentation method for the source training, which increases the model's resistance to potential domain shifts caused by diverse point densities.
- To enhance the model's scene comprehension, we design a multi-task learning with 3D scene restoration to boost the recognition and detection of objects during source training. Incorporating the 3D scene restoration task, we further utilize the lightweight parameter updates to adapt the model to unseen target domains during testing time, to further bridge domain gaps.
- Extensive cross-dataset experiments covering “Car”, “Pedestrian”, and “Cyclist” detections demonstrate our model outperforms the state-of-the-art DG methods and even overpass UDA methods under some circumstances.

2. Relate Work

2.1. Point-Cloud-Based 3D Object Detection

Point-cloud-based 3D object detection [1, 9, 30–32, 47] aims to locate and classify objects of interest in point clouds. Existing detection methods can be categorized into voxel-based and point-based. Voxel-based methods

[9, 18, 24, 47] voxelize point clouds into grid-like 3D images and use sparse convolution to extract abstract features for object detection, which are computationally efficient but may lose fine-grained details due to voxelization. The point-based methods [31, 34] extract abstract features directly from raw points, preserving fine-grained details but possessing relatively heavy computation. As a trade-off, some point-voxel-mixed methods [32, 33] combine raw points and voxels to balance representation learning and computation efficiency. In this article, we mainly focus on voxel-based object detection.

2.2. Domain Generalization on 2D/3D Object Detection

Domain generalization [16, 27, 39] aims to bridge domain shifts unseen during the source training but may encountered in the target testing. In 2D image tasks, domain generalization methods have been well explored and include data augmentation [39, 40], domain alignment learning [26, 27], meta-learning [2, 20], test-time adaptation [6, 16], *etc.* In the realm of 3D object detection, existing works [35, 45] mainly focus on multi-domain generalization. Wu *et al.* in [45] propose to align extracted features of detectors individually trained on multiple source domains to learn domain-invariant features. Soum-Fontez *et al.* in [35] utilize label re-annotation and cross-dataset instance injection to mitigate the performance degradation. However, regarding single-domain cases, although well-explored in 2D image detection [38, 44, 54], there has been relatively rare research in 3D object detection. Lehner *et al.* in [19] propose the adversarial augmentation to deal with rare-shape or broken cars. Choi *et al.* in [8] combine 5 basic augmentations to build the part-aware data augmentation to handle noise and locally missing points. Unlike prior works solely focusing on data augmentation, our work not only introduces a novel physical-aware data augmentation method, but also contributes a new multi-task learning framework.

2.3. Test-Time Adaptation in Domain Generalization

Testing-time adaptation [5, 22] refers to conducting adjustments or refinements to a model’s parameters or inferences during the testing or inference phase. Current methods include pseudo-labeling [7, 21], consistency training [41], self-supervised learning [5, 25], *etc.* Recently, the increasing attention has landed on using test-time adaptation to tackle the domain generalization problem in 2D tasks [5–7, 16, 21, 23] and 3D classification [25, 41]. To the best of our knowledge, our work is the first to apply the test-time adaptation to the SDG for 3D object detection.

3. Problem Formulation

3D object detection aims to detect objects of interest in 3D point clouds. A frame of point cloud \mathbf{X} is a set of points $p = [x^p, y^p, z^p]$, where $[x^p, y^p, z^p]$ denotes the 3D Cartesian coordinates of points. The object detection can be formulated as $f(\mathbf{X}) = \{\mathbf{b}_i\}_{i=1}^{N_{obj}}$, where $f(\cdot)$ denotes the detection model and N_{obj} is the number of detected 3D boxes in \mathbf{X} . \mathbf{b}_i denotes the i^{th} detected box, which contains the location $[x_i, y_i, z_i]$, the dimension $[w_i, h_i, l_i]$, the heading angle θ_i , the classification label c_i , and the confidence score s_i .

Domain generalization for 3D object detection aims to generalize the model $f(\cdot)$ trained on a well-labeled source-domain dataset $\{\mathbf{X}_j^s, \mathbf{B}_j^s\}_{j=1}^{N^s}$ to a unseen target domain $\{\mathbf{X}_j^t, \mathbf{B}_j^t\}_{j=1}^{N^t}$, where the superscript s and t denote the source and target domain respectively. Correspondingly, N^s and N^t denote the number of point clouds, and \mathbf{B}_j^s and \mathbf{B}_j^t denote the sets of 3D boxes. Note that in domain generalization, only the source-domain data is available for model training. The target-domain data is accessible during model evaluation/deployment only.

4. Methodology

Figure 3 presents the system diagram of the proposed DG solution on 3D point cloud data. During training on the source domain, the point-cloud data is augmented by our PDDA method. Then the augmented sample is fed into the multi-task learning scheme, where the auxiliary self-supervised task (i.e. 3D scene restoration) promotes the encoder to extract features for scene comprehension. During testing on the target domain, we utilize the auxiliary 3D scene restoration loss to update parameters in the encoder-decoder path to adapt the encoder to unseen target domains, to further bridge the domain gap. The test-time adapted encoder together with the frozen detection head is then exploited for the final object detection.

4.1. Physical-Aware Density-Resampling Data Augmentation

Point density plays a crucial role in 3D object detection. It is affected by several factors, including the distances between objects in relation to LiDAR sensors, inter-object occlusion, and different weather conditions. Furthermore, various types of LiDAR sensors can introduce variations in point density, which can negatively impact the model’s ability to generalize to unseen environments. It’s important to note that the variations in point density due to various factors may follow distinct physical constraints. For example, point density is inversely proportional to the imaging distance. Furthermore, for spinning sensors, different beam layers of the sensor can lead to varying uniform-distributed densities in the vertical direction. To address the domain-specific bias arising from variations in point densities, Hu

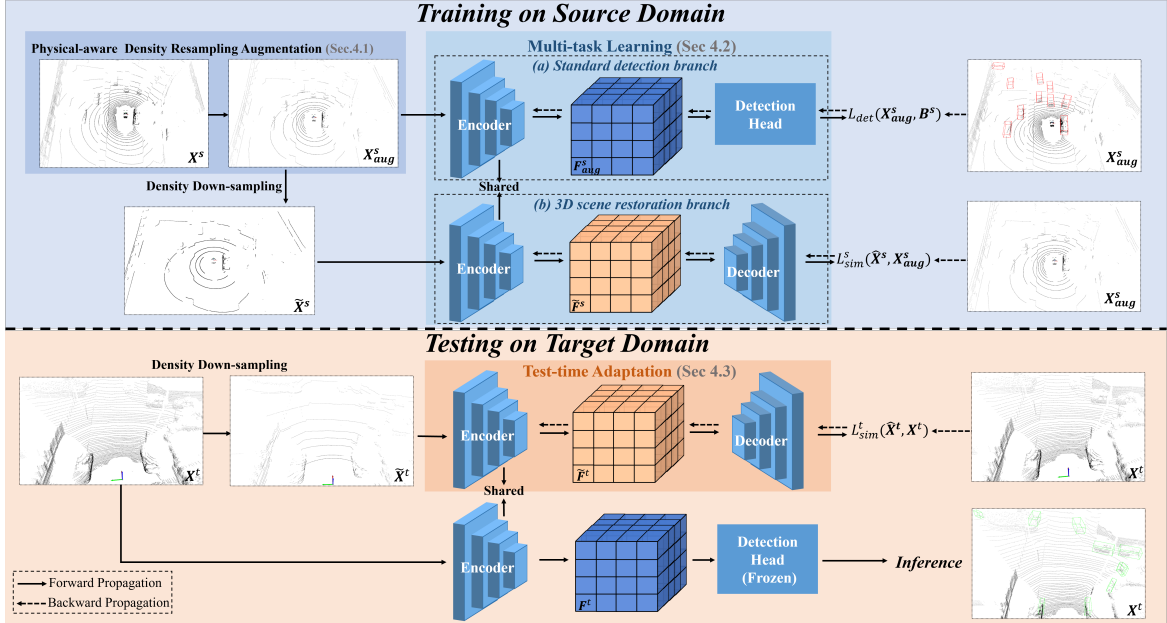


Figure 3. Pipeline of our proposed DG method. During training on the source domain, the training sample is augmented with density re-sampling, which is then used to train the multi-task model for (a) standard detection and (b) 3D scene restoration from its down-sampled version. During Testing on the target domain, given a query data, self-supervised scene restoration is conducted on the corresponding density-downsampled version for lightweight model update. Then the updated encoder works together with the frozen detection head for the final prediction. In this figure, source and target samples are from NuScenes [4] and KITTI [10], respectively.

et al. [15] proposed a random beam re-sampling (RBRs) method. Nonetheless, this solely randomly layer-sampling strategy does not adhere to the previously mentioned physical constraints, resulting in suboptimal outcomes. In this study, we design a physical-aware density-resampling data augmentation (PDDA) method to better simulate the real-world point cloud distribution, accounting for different density patterns.

Given the point clouds of the source dataset with M beam layers of LiDAR scanning, we first convert the Cartesian coordinates $[x, y, z]$ into spherical coordinates $[\gamma, \Theta, \Phi]$:

$$\gamma = \sqrt{x^2 + y^2 + z^2}, \Theta = \arctan \frac{y}{x}, \Phi = \arccos \frac{z}{\gamma}. \quad (1)$$

Considering the spinning beams commonly used in autonomous driving, we gather vertical angles $\{\Phi\}$ of points. After removing outliers of $\{\Phi\}$ (out of $3.1 \times$ standard deviation), we obtain the range of vertical angles $[\min\{\Phi\}, \max\{\Phi\}]$. Then we uniformly divide the range into M bins $[\Phi_k, \Phi_{k+1}]$ ($k \in \{1, 2, \dots, M\}$) and label points according to which bin the points land on. Then we perform our density-resampling data augmentation on source data by comprehensively considering physical-aware down-sampling and up-sampling.

To uniformly *down-sample* the density of the point cloud into a lower density, we keep one out of every C bins of

points. A higher value of C means a more severe reduction in density. Additionally, we remove points with a probability of P to simulate the global loss of laser reflections. To *up-sample* the density of the point cloud into a higher density, we adopt efficient linear interpolation to obtain new points. Specifically, new points will be interpolated by original points within two neighboring bins:

$$\eta_s^{new} = \lambda \eta_k + (1 - \lambda) \eta_{k+1} \quad (2)$$

s.t. $s \in \{1, 2, \dots, S-1\}$, $\lambda = \frac{s}{S}$,

where $\eta \in \{\gamma, \Theta, \Phi\}$ represents the spherical coordinate of points; k refers to points with Φ belonging to the k_{th} bins; s indicates the new points of s_{th} interpolated beam layer; λ is the interpolation ratio; the integer S ($S > 2$) is the interpolation factor and $S-1$ is the number of newly interpolated beam layers.

Considering low-density is relatively more detrimental to object detection than high-density, we select two down-sampling operations with $C \in \{2, 3\}$ (i.e., $2 \times$ *down-sampling* and $3 \times$ *down-sampling*) and one up-sampling operation with $S = 2$ ($2 \times$ *up-sampling*). At last, we design the universal density-resampling augmentation method operating on source training data, which randomly conducts one of $\{2 \times$ *down-sampling*, $3 \times$ *down-sampling*, *no-sampling*, $2 \times$ *up-sampling* $\}$ on each source point cloud

to simulate potential various densities on target domains. More visualizations are shown in Section 7 in the supplementary.

4.2. Multi-Task Learning with Density-Resampling

As shown in Figure 3, our multi-task learning scheme consists of the main standard detection task and the auxiliary self-supervised task. As we design, the auxiliary self-supervised task restores the globally uniformly masked points by density downsampling. Recently, some research [3, 53] has shown that background information is also crucial in object recognition and detection. Through our self-supervised task, the restoration of the 3D scene helps the encoder to better comprehend the background and foreground details of the scene, which benefits the model’s object recognition and thereby object detection.

Main standard detection task. By the PDDA in Section 4.1, we obtain the augmented point cloud \mathbf{X}_{aug}^s from the original point cloud \mathbf{X}^s . Then, we feed \mathbf{X}_{aug}^s into the encoder to obtain abstract features F_{aug} by $F_{aug} = f_{\theta_E}(\mathbf{X}_{aug}^s)$, where θ_E is the parameter of the encoder. Following the setting in [9], we calculate the standard detection loss \mathcal{L}_{det} :

$$\mathcal{L}_{det}(\mathbf{X}_{aug}^s, \mathbf{B}^s; \theta_E, \theta_H) = f_{\theta_H}(F_{aug}), \quad (3)$$

where θ_H is the parameter of the detection head.

Auxiliary self-supervised task. By density down-sampling in Section 4.1, we further down-sample \mathbf{X}_{aug}^s into $\tilde{\mathbf{X}}^s$. Then, we feed $\tilde{\mathbf{X}}^s$ into the encoder to obtain the abstract feature \tilde{F} by $\tilde{F} = f_{\theta_E}(\tilde{\mathbf{X}}^s)$. For 3D scene restoration, we use the decoder (symmetrical to the encoder) to restore the point cloud $\hat{\mathbf{X}}^s$ from \tilde{F} , namely $\hat{\mathbf{X}}^s = f_{\theta_D}(\tilde{F})$ where θ_D is the parameter of the decoder. To align $\hat{\mathbf{X}}^s$ with \mathbf{X}_{aug}^s , we first adopt the mean squared error (MSE) to calculate the \mathcal{L}_{mse}^s .

$$\mathcal{L}_{mse}^s(\tilde{\mathbf{X}}^s, \mathbf{X}_{aug}^s; \theta_E, \theta_D) = \|\hat{\mathbf{X}}^s - \mathbf{X}_{aug}^s\|_2^2. \quad (4)$$

To improve semantic similarity, we also leverage pre-trained PointNet++ [29] to acquire multi-scale abstract features of $\hat{\mathbf{X}}^s$ and \mathbf{X}_{aug}^s and calculate the perceptual loss [50]:

$$\begin{aligned} \mathcal{L}_{pcp}^s(\tilde{\mathbf{X}}^s, \mathbf{X}_{aug}^s; \theta_E, \theta_D) = & \\ & \sum_{i=1}^3 \mathcal{L}_{cos}(\text{PNet}_i(\hat{\mathbf{X}}^s), \text{PNet}_i(\mathbf{X}_{aug}^s)), \end{aligned} \quad (5)$$

where the cosine similarity loss $\mathcal{L}_{cos}(\mathbf{A}, \mathbf{B}) = 1 - \frac{\mathbf{A} \cdot \mathbf{B}}{\|\mathbf{A}\| \|\mathbf{B}\|}$ and $\text{PNet}_i(*) (i \in \{1, 2, 3\})$ outputs the flattened feature of the i_{th} block of the PointNet++ encoder. Thus, the compound loss of the self-supervised training \mathcal{L}_{self}^s ,

$$\mathcal{L}_{self}^s = \mathcal{L}_{mse}^s + \lambda_1 \mathcal{L}_{pcp}^s, \quad (6)$$

is used to restore the down-sampled point cloud for a better comprehension of the 3D scene.

Regarding the multi-task learning scheme, we adopt the two-stage training as in Figure 3: first, we conduct standard detection training to update the encoder and the detection head by \mathcal{L}_{det} and then utilize the self-supervised training to update the parameters of the decoder by \mathcal{L}_{self}^s . During the self-supervised training, we freeze the major trainable parameters of the encoder to ensure the output features aligned with the detection head and only update statistical parameters (*i.e.*, the mean and the standard deviation) of Batch-Norm layers to adapt the encoder to diverse feature styles given various densities.

4.3. Test-Time Adaptation with Self-Supervised 3D Scene Restoration

Prior research in the field of 2D domain generalization has shown that test-time adaptation can be a highly effective approach to mitigate the disparities between source and target domains [6, 16, 23]. It utilizes lightweight test-time optimization to adjust the model’s parameters during the testing. Nevertheless, this strategy has yet to be explored in the context of domain generalization of 3D point-cloud-based object detection.

Given the query data from an unseen domain, the effectiveness of test-time adaptation hinges on the proper construction of self-supervised learning. In this study, we make use of the auxiliary 3D scene restoration task proposed in our multi-task learning to adapt the parameters of the encoder to the target domain. Specifically, given a point cloud \mathbf{X}^t in the target domain, we first down-sample \mathbf{X}^t with the proposed PDDA augmentation, obtaining $\tilde{\mathbf{X}}^t$. Then $\tilde{\mathbf{X}}^t$ is interpolated by the encoder and decoder trained on the source data and the corresponding restoration loss

$$\mathcal{L}_{mse}^t(\tilde{\mathbf{X}}^t, \mathbf{X}^t; \theta_E, \theta_D) = \|f_{\theta_D}(f_{\theta_E}(\tilde{\mathbf{X}}^t)) - \mathbf{X}^t\|_2^2 \quad (7)$$

is used to update θ_E, θ_D , improving the encoder’s comprehension of the query scene. One may notice that the perceptual loss in (6) is omitted in our test-time adaptation, even though it leads to a marginal improvement in test-time optimization. This decision was made due to the significant computational latency introduced by the perceptual loss. We show this trade-off in Table 6 in the Supplementary.

During testing time, for each query data, we reset the parameters θ_E and θ_D to the initial state produced in the source training phase. We then iteratively update them a specific number of times, denoted as N_{iter} , to minimize the point-cloud restoration loss \mathcal{L}_{mse}^t . This approach ensures both high computational efficiency and detection performance improvement. After undergoing N_{iter} updates using the data from point cloud \mathbf{X}^t , the encoder is combined with the detection head to produce the final detection result.

Table 1. The overview of 3D point cloud datasets

Dataset	Frame	LiDAR Sensor	Vertical View
Waymo[36]	200K	1 x 64 spinning-beam + 4 x 200 fixed-beam	[-17.6, 2.4]
KITTI[10]	15K	1 x 64 spinning-beam	[-24.9, 2.0]
NuScenes[4]	40K(Labeled)	1 x 32 spinning-beam	[-30.0, 10.0]

5. Experiment

5.1. Experiment Settings

Datasets and metrics. We select three widely-recognized datasets of autonomous driving: KITTI [10], Waymo [36], NuScenes [4], as shown in Table 1. KITTI contains $\sim 15K$ frames of point clouds collected by a spinning 64-beam LiDAR. Waymo comprises $\sim 200K$ frames collected by one 64-beam spinning LiDAR and four 200-beam fixed LiDARs. For Waymo samples collected continuously over time, we evenly sample 20% of them for experiments. NuScenes contains $\sim 40K$ labeled key-frames. Three datasets present shifted distributions caused by different LiDAR types, geographic collection locations, inconsistent object sizes, *etc.* Following conventional settings in [15, 48, 49], we evaluate models under cross-dataset settings of NuScenes \rightarrow KITTI, Waymo \rightarrow NuScenes, and Waymo \rightarrow KITTI. We select “Car” (also “Vehicle” in Waymo), “Pedestrian” and “Cyclist” (also “bicycle” in NuScenes) for detection. For the fair evaluation across datasets, we take the average precision (AP) of 40 recalls and the mean AP (mAP) averaging on all object classes on both 3D and BEV views as the evaluation metrics. The IoU thresholds are 0.7 for “Car” and 0.5 for “Pedestrian” and “Cyclist”. Note that, for KITTI, we record the average AP at all difficulty levels (*i.e.*, Easy, Moderate, and Hard).

Implementation details. We evaluate all DG and UDA methods based on the powerful detector VoxelRCNN [9] which uses voxel-based features for both representation extraction and box refinement. For a fair comparison, we use the single unified VoxelRCNN simultaneously detecting “Car”, “Pedestrian”, and “Cyclist”. We conduct the experiments on the popular codebase openpcdet [37] and openpcdet-based Uni3D [52]. For the source training, we adopt the down-sampling with $C \in \{3, 4, 6\}$ and the one-cycle Adam optimizer with a learning rate of 0.01 during 30 training epochs. Due to unreachable labeled target data, we select the best checkpoint through the validation with labeled source *val* data. For self-supervised learning, we finetune the model for a limited 5 epochs with $\lambda_1 = 1.0$. We also adopt common data augmentations for all detections, including random world flipping, random world scaling, random world rotation, and ground-truth object sampling. For the test-time training, we adopt the down-sampling with $C \in \{6, 8\}$, the Adam optimizer

with a learning rate of 0.001 and set $N_{iter} = 5$ for each sample. Regarding no prior information on the target domain, we set the number of beam layers as the default 64. Using $2 \times$ GeForce RTX-3090/A100, we set the batch size to 4 in source training and 1 in test-time training following the real-world online frame-flow input. For the consistent format of point clouds across datasets, we unify the LiDAR coordinate system with the origin on the ground within the range of $[-75.2m, -75.2m, -2m, 75.2m, 75.2m, 4m]$ and the voxel size of $[0.1m, 0.1m, 0.15m]$.

Compared methods. (a) DG methods: 3D-VF [19] leverages the adversarial vector-field-based augmentation to generalize the detector to the rare-shape or broken objects. PA-DA [8] utilizes the part-aware data augmentation combining 5 basic augmentation methods (*i.e.*, $\{dropout, swap, mix, sparse, noise\}$) to enable the detector robust to noise and dropout points. (b) UDA methods: SN [42] leverages data augmentation to de-bias the impact of different object sizes on model generalization. Incorporating random object scaling (ROS), ST3D++ [49] designs a self-training pipeline to improve the quality of pseudo-labels of unlabeled target-domain data for cross-domain adaptation. The implementation details can be referred to Section 8.1 in the supplementary.

5.2. Comparison with SOTA Methods

Comparison among DG methods. For DG settings, our method outperforms the compared methods, as shown in Table 2. Specifically, for NuScenes \rightarrow KITTI and Waymo \rightarrow NuScenes where significant low-to-high-density and high-to-low-density domain gaps exist, compared with the second-best performance, the mAPs of our method have increased by ratios of 12.60%/8.73% and 21.61%/20.30% (with mAP increases of 4.72%/2.02% and 3.06%/1.90%). It demonstrates our method’s generalizability to various density-related domain gaps. 3D-VF and PA-DA aim to overcome the bias caused by the rare-shape objects and noisy and locally missing points. However, due to the ignorance of the point layer variation by different sensors, they lead to limited detection performance. For Waymo \rightarrow KITTI with no significant density-related domain gap, our method still improves the detection accuracy on “Car” objects where the bias of object size exists considering “Car” in KITTI *v.s.* “Vehicle” (including trunks, vans, *etc.*) in Waymo, which indicates our method’s improvement on the model’s generalizability to unseen object sizes.

Comparison with UDA methods. The UDA methods leverage reachable unlabeled data and relevant knowledge on the target domain to improve the detection of target domain data. SN aims to normalize object sizes to the target domain, and ST3D++ utilizes ROS augmentation to make the model adaptable to various object sizes. Hence, as shown in Table 2, these two methods perform best on

Table 2. Performance comparison of different methods on DG and UDA tasks. The values on both sides respectively represent the APs on BEV and 3D views (*i.e.*, AP_{BEV}/AP_{3D}). The bold **values** represent the best performance in DG tasks and the underlined values for the best performance in DG + UDA tasks. “Source-only” represents the standard detection model trained by source data without DG, UDA, or additional augmentation methods.

Tasks	Methods	Car	Pedestrian	Cyclist	mAP	
NuScenes \rightarrow KITTI	DG	Source-only PA-DA[8] 3D-VF[19] Ours	62.69/19.02 65.09/32.44 65.36/29.21 73.58/33.11	22.72/18.37 18.73/14.94 24.85/20.87 30.01/23.73	20.61/18.13 18.66/15.91 22.13/ 19.31 22.93/18.62	35.34/18.5 34.16/21.1 37.45/23.13 42.17/25.15
	UDA	SN[42] ST3D++[49]	70.5/54.78 <u>83.57/64.17</u>	19.71/15.42 29.27/ <u>25.07</u>	13.36/10.83 16.61/16.12	34.52/27.01 <u>43.15/35.12</u>
	DG	Source-only PA-DA[8] 3D-VF[19] Ours	31.2/19.13 29.43/18.06 30.17/18.91 36.04/22.25	10.52/8.39 10.84/8.43 10.54/7.23 14.48/10.56	0.75/0.55 0.82/0.43 0.76/0.78 1.15/0.95	14.16/9.36 13.7/8.97 13.82/8.97 17.22/11.26
	UDA	SN[42] ST3D++[49]	29.32/18.84 27.58/20.25	12.72/ <u>10.57</u> 11.88/9.44	0.72/0.45 0.01/0.01	14.25/9.96 13.15/9.9
Waymo \rightarrow NuScenes	DG	Source-only PA-DA[8] 3D-VF[19] Ours	66.65/19.27 65.82/17.61 66.72/19.37 69.9/20.21	66.55/64.00 66.40/63.88 66.21/63.12 63.24/62.59	63.04/57.11 61.30/56.23 62.74/56.44 63.27/57.21	65.41/ 46.79 64.51/45.91 65.22/46.31 65.47/46.67
	UDA	SN[42] ST3D++[49]	72.43/49.34 <u>83.59/60.63</u>	<u>71.08/69.35</u> 50.18/48.4	56.00/53.02 52.61/47.38	<u>66.51/57.23</u> 62.13/52.14

NuScenes \rightarrow KITTI and Waymo \rightarrow KITTI with noticeable domain gaps related to object size, especially for “Car” objects. However, on Waymo \rightarrow NuScenes where there is no significant difference in object size, density-related domain gaps dominate. For Waymo \rightarrow NuScenes, our method outperforms SN and ST3D++ and reaches the best performance.

5.3. Ablation Study

In this section, we conduct extensive ablation experiments to investigate the individual components of our proposed DG method. All ablation studies are conducted on NuScenes \rightarrow KITTI and Waymo \rightarrow NuScenes and use the VoxelRCNN as the basic detection model. More detailed results are shown in Section 8.2 in the supplementary.

Component ablation. As demonstrated in Table 3, we investigate the effectiveness of our individual components. Compared with (a) the detection model only trained with source domain data, (b) applying PDDA augmentation during source training brings significant improvement. By means of (c) multi-task learning, the detection rate has a slight boost. In the end, (d) the adoption of test-time adaptation further improves the performance.

Comparison on data augmentation. Besides the DG augmentation methods (*i.e.*, PA-DA [8] and 3D-VF [19]), we also include the weather-simulating augmentation methods Rain [17] and Fog [11] which simulate the adverse rain and fog in point clouds. As shown in Table 4, our

Table 3. Component ablations in mAP(%). **Source** represents the conventional training procedure. **PDDA**, **MTL** and **TTA** represent our data augmentation, multi-task learning, and test-time adaptation, respectively.

	Source	PDDA	MTL	TTA	N \rightarrow K	W \rightarrow N
(a)	✓				35.34/18.5	14.16/9.36
(b)	✓	✓			41.07/24.08	16.83/11.04
(c)	✓	✓	✓		41.35/24.12	17.09/11.17
(d)	✓	✓	✓	✓	42.17/25.15	17.22/11.26

PDDA method outperforms all compared DG augmentation methods. In this ablation, we also include UDA augmentation methods that require target-domain information: SN [42], RBRS [15], and ROS [48, 49]. Particularly, for density-related domain shifts, RBRS [15] employs random upsampling on the low-to-high-density NuScenes \rightarrow KITTI and downsampling on the high-to-low-density Waymo \rightarrow NuScenes. For a comparison, without relying on target domain information, our PDDA outperforms RBRS on NuScenes \rightarrow KITTI and closely approximates RBRS on Waymo \rightarrow NuScenes (with a slight 0.5%/0.16% lag), which indicates the superiority of PDDA’s capturing the physical-aware characteristics of real-world beam layer scanning.

Comparison on test-time training. To further explore the performance of our proposed test-time training, following the Point-MATE [25], we adopt the masking strategy based on K nearest neighbors (KNN) with the masking rate

Table 4. Data augmentation ablations in mAP(%). The bold **values** represent the best performance in DG tasks and the underlined values for the best performance in DG + UDA tasks.

Tasks	Methods	N→K	W→N
DG	Source-only	35.34/18.50	14.16/9.36
	PA-DA[8]	34.16/21.10	13.70/8.97
	3D-VF[19]	37.45/23.13	13.82/8.97
	Fog[11]	38.99/23.01	14.59/9.43
	Rain[17]	37.04/23.12	15.21/9.86
	PDDA	41.07/24.08	16.83/11.04
UDA	RBRS[15]	39.21/20.82	<u>17.33/11.20</u>
	SN[42]	34.52/27.01	14.25/9.96
	ROS[49]	38.18/28.29	13.67/8.86

Table 5. Comparison on test-time training. KNN-TTT stands for applying the KNN-based masking strategy during self-supervised training and test-time training, instead of density-downsampling as in our proposed method. FPS stands for the number of frames processed by the detection model per second.

Methods	N→K		W→N	
	mAP (%)	computation (FPS)	mAP (%)	computation (FPS)
KNN-TTT[25]	40.51/24.92	0.52	16.67/11.03	0.41
Our TTT	42.17/25.15	4.23	17.22/11.26	3.52

of 90% during self-supervised training and test-time training (refer to implementation details in Section 8.1 in the supplementary). As shown in Table 5, while the KNN-masking-based test-time training reaches approximate accuracy to our density-downsampling-based method (with a slight lag), the computation of farthest point sampling and KNN clustering on all points cause the severe latency. In contrast, our density-sampling operations on points perform more accurately and more efficiently on object detection.

Computation efficiency. We explore the computation efficiency w.r.t. processing of a single GeForce RTX-3090 GPU. As shown in Figure 4, the optimal N_{iter} reaching the best performance are 10 for NuScenes → KITTI and 20 for Waymo → NuScenes. After that, the detection performance gets worse due to the model overfitting to the auxiliary task. Given such N_{iter} settings, the real-time processing requires parallel computation with multiple GPUs. For the single-GPU setting, the computation speed with $N_{iter} = 5$ still overpasses the 2 FPS labeled keyframe rate of NuScenes. By a minor performance penalty, the computation speed with $N_{iter} = 1$ meets the 10 FPS real-time running requirement of Waymo, and the accuracy (41.41%/24.19% on NuScenes → KITTI and 17.00%/11.16%) still overpass other DG methods in Table 2.

5.4. Limitation

As shown in Table 2, our proposed method improves the model’s generalizability on density-variation-related set-

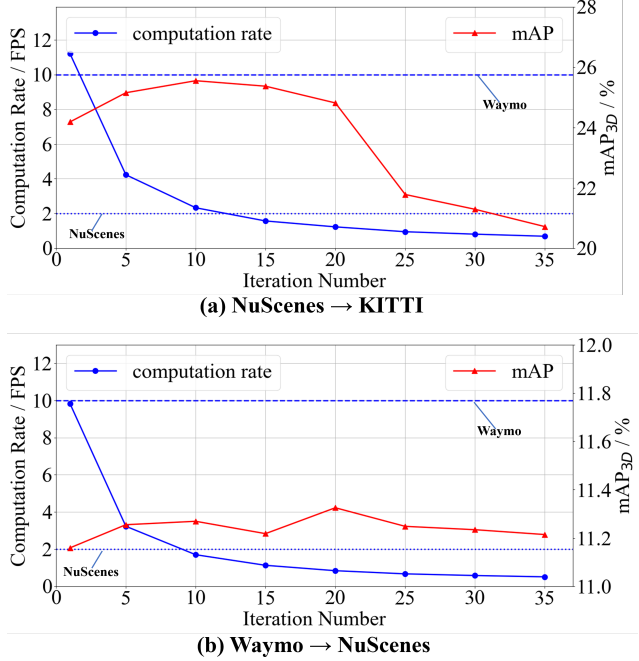


Figure 4. Computation efficiency on (a) NuScenes → KITTI and (b) Waymo → NuScenes. We indicate Waymo’s frame rate of 10 FPS and NuScenes’s keyframe rate of 2 FPS by dash lines.

tings, e.g. NuScenes → KITTI, Waymo → NuScenes, and “Car” detection on Waymo → KITTI where object size bias exists. However, regarding tasks with no significant domain shifts, such as “Pedestrian” and “Cyclist” detection on Waymo → KITTI, our method brings no or minor improvement in detection accuracy, which is a topic we plan to solve in the future.

6. Conclusion

Point-cloud-based 3D object detection suffers from performance degradation when encountering data with unexplored domain gaps. To tackle this problem, we proposed the domain generalization method to improve the model’s generalizability. We first designed a physical-aware density-based data augmentation to mitigate the performance loss stemming from diverse point densities. From the learning methodology viewpoint, we introduced a multi-task learning solution, incorporating self-supervised 3D scene restoration into the object detection task. Beyond the model optimization benefit in source-domain training, the self-supervised restoration task is also used for the test-time update of the encoder for feature extraction. As the first test-time adaptation solution on domain generalization of 3D point-cloud-based object detection, our method significantly improves the detection model’s performance to unseen target domains.

References

[1] Eduardo Arnold, Omar Y Al-Jarrah, Mehrdad Dianati, Saber Fallah, David Oxtoby, and Alex Mouzakitis. A survey on 3d object detection methods for autonomous driving applications. *IEEE Transactions on Intelligent Transportation Systems*, 20(10):3782–3795, 2019. [1](#), [2](#)

[2] Yogesh Balaji, Swami Sankaranarayanan, and Rama Chellappa. Metareg: Towards domain generalization using meta-regularization. *Advances in neural information processing systems*, 31, 2018. [3](#)

[3] Susan J Boyce, Alexander Pollatsek, and Keith Rayner. Effect of background information on object identification. *Journal of Experimental Psychology: Human Perception and Performance*, 15(3):556, 1989. [2](#), [5](#)

[4] Holger Caesar, Varun Bankiti, Alex H Lang, Sourabh Vora, Venice Erin Liang, Qiang Xu, Anush Krishnan, Yu Pan, Giacarlo Baldan, and Oscar Beijbom. muscenes: A multimodal dataset for autonomous driving. In *Proceedings of the IEEE/CVF conference on computer vision and pattern recognition*, pages 11621–11631, 2020. [4](#), [6](#)

[5] Dian Chen, Dequan Wang, Trevor Darrell, and Sayna Ebrahimi. Contrastive test-time adaptation. In *Proceedings of the IEEE/CVF Conference on Computer Vision and Pattern Recognition*, pages 295–305, 2022. [3](#)

[6] Liang Chen, Yong Zhang, Yibing Song, Ying Shan, and Lingqiao Liu. Improved test-time adaptation for domain generalization. In *Proceedings of the IEEE/CVF Conference on Computer Vision and Pattern Recognition*, pages 24172–24182, 2023. [3](#), [5](#)

[7] Weijie Chen, Luojun Lin, Shicai Yang, Di Xie, Shiliang Pu, and Yuetong Zhuang. Self-supervised noisy label learning for source-free unsupervised domain adaptation. In *2022 IEEE/RSJ International Conference on Intelligent Robots and Systems (IROS)*, pages 10185–10192. IEEE, 2022. [3](#)

[8] Jaeseok Choi, Yeji Song, and Nojun Kwak. Part-aware data augmentation for 3d object detection in point cloud. In *2021 IEEE/RSJ International Conference on Intelligent Robots and Systems (IROS)*, pages 3391–3397. IEEE, 2021. [1](#), [2](#), [3](#), [6](#), [7](#), [8](#)

[9] Jiajun Deng, Shaoshuai Shi, Peiwei Li, Wengang Zhou, Yanyong Zhang, and Houqiang Li. Voxel r-cnn: Towards high performance voxel-based 3d object detection. In *Proceedings of the AAAI Conference on Artificial Intelligence*, pages 1201–1209, 2021. [2](#), [3](#), [5](#), [6](#)

[10] Andreas Geiger, Philip Lenz, Christoph Stiller, and Raquel Urtasun. Vision meets robotics: The kitti dataset. *The International Journal of Robotics Research*, 32(11):1231–1237, 2013. [4](#), [6](#)

[11] Martin Hahner, Christos Sakaridis, Dengxin Dai, and Luc Van Gool. Fog simulation on real lidar point clouds for 3d object detection in adverse weather. In *Proceedings of the IEEE/CVF International Conference on Computer Vision*, pages 15283–15292, 2021. [1](#), [2](#), [7](#), [8](#)

[12] Martin Hahner, Christos Sakaridis, Mario Bijelic, Felix Heide, Fisher Yu, Dengxin Dai, and Luc Van Gool. Lidar snowfall simulation for robust 3d object detection. In *Proceedings of the IEEE/CVF Conference on Computer Vision and Pattern Recognition*, pages 16364–16374, 2022. [1](#), [2](#)

[13] Marcus Hammer, Marcus Hebel, Martin Laurenzis, and Michael Arens. Lidar-based detection and tracking of small uavs. In *Emerging Imaging and Sensing Technologies for Security and Defence III; and Unmanned Sensors, Systems, and Countermeasures*, pages 177–185. SPIE, 2018. [1](#)

[14] Jordan SK Hu, Tianshu Kuai, and Steven L Waslander. Point density-aware voxels for lidar 3d object detection. In *Proceedings of the IEEE/CVF Conference on Computer Vision and Pattern Recognition*, pages 8469–8478, 2022. [2](#)

[15] Qianjiang Hu, Daizong Liu, and Wei Hu. Density-insensitive unsupervised domain adaption on 3d object detection. In *Proceedings of the IEEE/CVF Conference on Computer Vision and Pattern Recognition*, pages 17556–17566, 2023. [1](#), [4](#), [6](#), [7](#), [8](#), [2](#)

[16] Yusuke Iwasawa and Yutaka Matsuo. Test-time classifier adjustment module for model-agnostic domain generalization. *Advances in Neural Information Processing Systems*, 34:2427–2440, 2021. [1](#), [3](#), [5](#)

[17] Velat Kilic, Deepti Hegde, Vishwanath Sindagi, A Brinton Cooper, Mark A Foster, and Vishal M Patel. Lidar light scattering augmentation (llsa): Physics-based simulation of adverse weather conditions for 3d object detection. *arXiv preprint arXiv:2107.07004*, 2021. [1](#), [2](#), [7](#), [8](#)

[18] Alex H Lang, Sourabh Vora, Holger Caesar, Lubing Zhou, Jiong Yang, and Oscar Beijbom. Pointpillars: Fast encoders for object detection from point clouds. In *Proceedings of the IEEE/CVF conference on computer vision and pattern recognition*, pages 12697–12705, 2019. [3](#)

[19] Alexander Lehner, Stefano Gasperini, Alvaro Marcos-Ramiro, Michael Schmidt, Mohammad-Ali Nikouei Mahani, Nassir Navab, Benjamin Busam, and Federico Tombari. 3d-vfield: Adversarial augmentation of point clouds for domain generalization in 3d object detection. In *Proceedings of the IEEE/CVF Conference on Computer Vision and Pattern Recognition*, pages 17295–17304, 2022. [1](#), [2](#), [3](#), [6](#), [7](#), [8](#)

[20] Da Li, Yongxin Yang, Yi-Zhe Song, and Timothy Hospedales. Learning to generalize: Meta-learning for domain generalization. In *Proceedings of the AAAI conference on artificial intelligence*, 2018. [3](#)

[21] Jian Liang, Dapeng Hu, and Jiashi Feng. Do we really need to access the source data? source hypothesis transfer for unsupervised domain adaptation. In *International conference on machine learning*, pages 6028–6039. PMLR, 2020. [3](#)

[22] Jian Liang, Ran He, and Tieniu Tan. A comprehensive survey on test-time adaptation under distribution shifts. *arXiv preprint arXiv:2303.15361*, 2023. [3](#)

[23] Quande Liu, Cheng Chen, Qi Dou, and Pheng-Ann Heng. Single-domain generalization in medical image segmentation via test-time adaptation from shape dictionary. In *Proceedings of the AAAI Conference on Artificial Intelligence*, pages 1756–1764, 2022. [3](#), [5](#)

[24] Jiageng Mao, Yujing Xue, Minzhe Niu, Haoyue Bai, Jiashi Feng, Xiaodan Liang, Hang Xu, and Chunjing Xu. Voxel transformer for 3d object detection. In *Proceedings of the IEEE/CVF International Conference on Computer Vision*, pages 3164–3173, 2021. [3](#)

[25] M Jehanzeb Mirza, Inkyu Shin, Wei Lin, Andreas Schriebl, Kunyang Sun, Jaesung Choe, Mateusz Kozinski, Horst Possegger, In So Kweon, Kuk-Jin Yoon, et al. Mate: Masked autoencoders are online 3d test-time learners. In *Proceedings of the IEEE/CVF International Conference on Computer Vision*, pages 16709–16718, 2023. 3, 7, 8, 2

[26] Saeid Motian, Marco Piccirilli, Donald A Adjeroh, and Gi-anfranco Doretto. Unified deep supervised domain adaptation and generalization. In *Proceedings of the IEEE international conference on computer vision*, pages 5715–5725, 2017. 3

[27] Krikamol Muandet, David Balduzzi, and Bernhard Schölkopf. Domain generalization via invariant feature representation. In *International conference on machine learning*, pages 10–18. PMLR, 2013. 1, 3

[28] Cheng Ouyang, Chen Chen, Surui Li, Zeju Li, Chen Qin, Wenjia Bai, and Daniel Rueckert. Causality-inspired single-source domain generalization for medical image segmentation. *IEEE Transactions on Medical Imaging*, 42(4):1095–1106, 2022. 2

[29] Charles Ruizhongtai Qi, Li Yi, Hao Su, and Leonidas J Guibas. Pointnet++: Deep hierarchical feature learning on point sets in a metric space. *Advances in neural information processing systems*, 30, 2017. 5

[30] Rui Qian, Xin Lai, and Xirong Li. 3d object detection for autonomous driving: A survey. *Pattern Recognition*, 130: 108796, 2022. 1, 2

[31] Shaoshuai Shi, Xiaogang Wang, and Hongsheng Li. Pointrcnn: 3d object proposal generation and detection from point cloud. In *Proceedings of the IEEE/CVF conference on computer vision and pattern recognition*, pages 770–779, 2019. 1, 3

[32] Shaoshuai Shi, Chaoxu Guo, Li Jiang, Zhe Wang, Jianping Shi, Xiaogang Wang, and Hongsheng Li. Pv-rcnn: Point-voxel feature set abstraction for 3d object detection. In *Proceedings of the IEEE/CVF conference on computer vision and pattern recognition*, pages 10529–10538, 2020. 2, 3

[33] Shaoshuai Shi, Li Jiang, Jiajun Deng, Zhe Wang, Chaoxu Guo, Jianping Shi, Xiaogang Wang, and Hongsheng Li. Pv-rcnn++: Point-voxel feature set abstraction with local vector representation for 3d object detection. *International Journal of Computer Vision*, 131(2):531–551, 2023. 3

[34] Weijing Shi and Raj Rajkumar. Point-gnn: Graph neural network for 3d object detection in a point cloud. In *Proceedings of the IEEE/CVF conference on computer vision and pattern recognition*, pages 1711–1719, 2020. 3

[35] Louis Soum-Fontez, Jean-Emmanuel Deschaud, and François Goulette. Mdt3d: Multi-dataset training for lidar 3d object detection generalization. *arXiv preprint arXiv:2308.01000*, 2023. 1, 3

[36] Pei Sun, Henrik Kretzschmar, Xerxes Dotiwalla, Aurelien Chouard, Vijaysai Patnaik, Paul Tsui, James Guo, Yin Zhou, Yuning Chai, Benjamin Caine, et al. Scalability in perception for autonomous driving: Waymo open dataset. In *Proceedings of the IEEE/CVF conference on computer vision and pattern recognition*, pages 2446–2454, 2020. 6

[37] OpenPCDet Development Team. Openpcdet: An open-source toolbox for 3d object detection from point clouds. <https://github.com/open-mmlab/OpenPCDet>, 2020. 6

[38] Vudit Vudit, Martin Engilberge, and Mathieu Salzmann. Clip the gap: A single domain generalization approach for object detection. In *Proceedings of the IEEE/CVF Conference on Computer Vision and Pattern Recognition*, pages 3219–3229, 2023. 2, 3

[39] Riccardo Volpi and Vittorio Murino. Addressing model vulnerability to distributional shifts over image transformation sets. In *Proceedings of the IEEE/CVF International Conference on Computer Vision*, pages 7980–7989, 2019. 1, 3

[40] Riccardo Volpi, Hongseok Namkoong, Ozan Sener, John C Duchi, Vittorio Murino, and Silvio Savarese. Generalizing to unseen domains via adversarial data augmentation. *Advances in neural information processing systems*, 31, 2018. 3

[41] Dequan Wang, Evan Shelhamer, Shaoteng Liu, Bruno Olshausen, and Trevor Darrell. Tent: Fully test-time adaptation by entropy minimization. *arXiv preprint arXiv:2006.10726*, 2020. 3

[42] Yan Wang, Xiangyu Chen, Yurong You, Li Erran Li, Bharath Hariharan, Mark Campbell, Kilian Q Weinberger, and Wei-Lun Chao. Train in germany, test in the usa: Making 3d object detectors generalize. In *Proceedings of the IEEE/CVF Conference on Computer Vision and Pattern Recognition*, pages 11713–11723, 2020. 1, 6, 7, 8, 2

[43] Zijian Wang, Yadan Luo, Ruihong Qiu, Zi Huang, and Mahsa Baktashmotagh. Learning to diversify for single domain generalization. In *Proceedings of the IEEE/CVF International Conference on Computer Vision*, pages 834–843, 2021. 2

[44] Aming Wu and Cheng Deng. Single-domain generalized object detection in urban scene via cyclic-disentangled self-distillation. In *Proceedings of the IEEE/CVF Conference on computer vision and pattern recognition*, pages 847–856, 2022. 3

[45] Guile Wu, Tongtong Cao, Bingbing Liu, Xingxin Chen, and Yuan Ren. Towards universal lidar-based 3d object detection by multi-domain knowledge transfer. In *Proceedings of the IEEE/CVF International Conference on Computer Vision*, pages 8669–8678, 2023. 1, 3

[46] Qiangeng Xu, Yiqi Zhong, and Ulrich Neumann. Behind the curtain: Learning occluded shapes for 3d object detection. In *Proceedings of the AAAI Conference on Artificial Intelligence*, pages 2893–2901, 2022. 2

[47] Yan Yan, Yuxing Mao, and Bo Li. Second: Sparsely embedded convolutional detection. *Sensors*, 18(10):3337, 2018. 1, 2, 3

[48] Jihan Yang, Shaoshuai Shi, Zhe Wang, Hongsheng Li, and Xiaojuan Qi. St3d: Self-training for unsupervised domain adaptation on 3d object detection. In *Proceedings of the IEEE/CVF conference on computer vision and pattern recognition*, pages 10368–10378, 2021. 6, 7

[49] Jihan Yang, Shaoshuai Shi, Zhe Wang, Hongsheng Li, and Xiaojuan Qi. St3d++: denoised self-training for unsupervised domain adaptation on 3d object detection. *arXiv preprint arXiv:2108.06682*, 2021. 1, 6, 7, 8, 2

[50] Qingsong Yang, Pingkun Yan, Yanbo Zhang, Hengyong Yu, Yongyi Shi, Xuanqin Mou, Mannudeep K Kalra, Yi Zhang, Ling Sun, and Ge Wang. Low-dose ct image denoising using a generative adversarial network with wasserstein distance and perceptual loss. *IEEE transactions on medical imaging*, 37(6):1348–1357, 2018. 5

[51] Yangyang Ye, Houjin Chen, Chi Zhang, Xiaoli Hao, and Zhaoxiang Zhang. Sarpnet: Shape attention regional proposal network for lidar-based 3d object detection. *Neurocomputing*, 379:53–63, 2020. 1

[52] Bo Zhang, Jiakang Yuan, Botian Shi, Tao Chen, Yikang Li, and Yu Qiao. Uni3d: A unified baseline for multi-dataset 3d object detection. In *Proceedings of the IEEE/CVF Conference on Computer Vision and Pattern Recognition*, pages 9253–9262, 2023. 6

[53] Yu Zheng, Yueqi Duan, Jiwen Lu, Jie Zhou, and Qi Tian. Hyperdet3d: Learning a scene-conditioned 3d object detector. In *Proceedings of the IEEE/CVF Conference on Computer Vision and Pattern Recognition*, pages 5585–5594, 2022. 2, 5

[54] Kaiyang Zhou, Ziwei Liu, Yu Qiao, Tao Xiang, and Chen Change Loy. Domain generalization: A survey. *IEEE Transactions on Pattern Analysis and Machine Intelligence*, 2022. 2, 3

Domain Generalization of 3D Object Detection by Density-Resampling

Supplementary Material

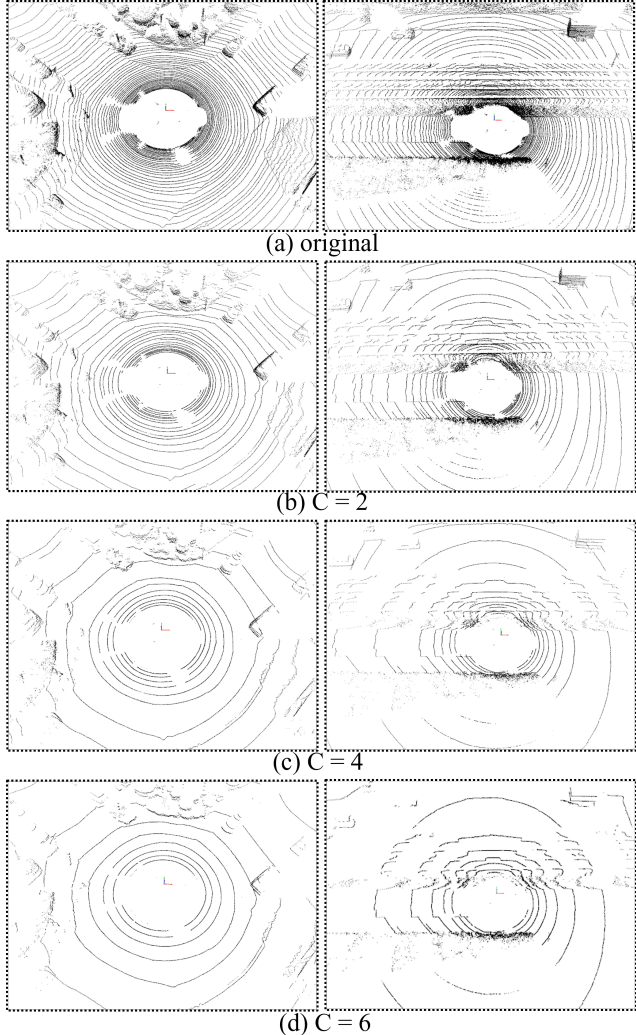


Figure 5. Visualization of density down-sampling.

In this supplementary section, we present the visualizations of our proposed PDDA in Section 7 and provide more specifics for the experiment implementation and comparison results in Section 8.

7. Physical-aware Density-resampling Data Augmentation

In Section 4.1, we design a universal physical-aware density-based data augmentation (PDDA) method by simulating real-world diverse uniformly distributed beam layers of different types of sensors. For a clear visualization of PDDA’s realistic point imaging, we present the density-

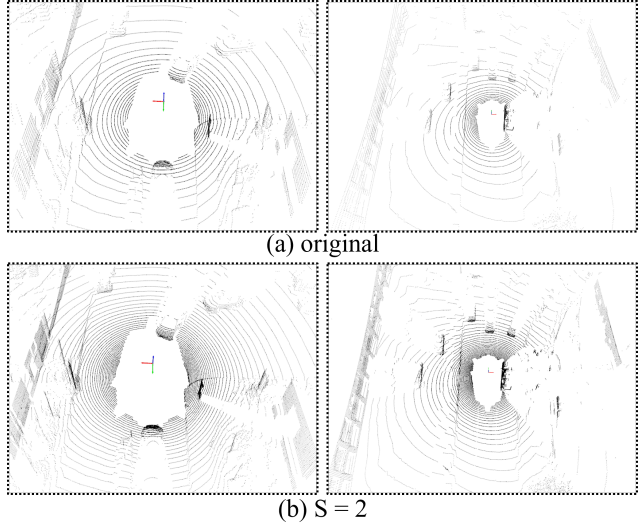


Figure 6. Visualization of density up-sampling.

Table 6. Effects of the perceptual loss on detection performance

Losses	N→K		W→N	
	mAP (%)	computation (FPS)	mAP (%)	computation (FPS)
Perceptual + MSE	42.21/25.16	0.89	17.20/11.36	0.78
MSE	42.17/25.15	4.23	17.22/11.26	3.52

downsampling on the 64-beam KITTI point clouds and density-upsampling on the 32-beam NuScenes point clouds. As shown in Figures 5 and 6, our PDDA augmentation simulates the realistic point clouds with various uniformly distributed point layers.

8. Experiment

In this section, we present readers with more implementation specifics about the compared DG and UDA methods in Section 8.1 and show more detailed evaluation results on the detection of “Car”, “Pedestrian”, and “Cyclist” in Section 8.2.

8.1. Experiment Implementation

Regarding compared methods shown in Sections 5.2 and 5.3, we all apply them on a single unified VoxelRCNN model to simultaneously detect “Car”, “Pedestrian”, and “Cyclist” for the fair comparison. By following the recommended settings in the papers, we implement them for the ablation comparison study:

- **3D-VF**: Due to the lack of the released code, we reimplement 3D-VF by following instructions in [19], and apply it to objects of pedestrians and cyclists. As indicated in [19], the augmentation by 3D-VF only randomly selects one object for each object class and perturbs its points in the point cloud.
- **PA-DA**: As the recommended settings in [8], we set the parameter of augmentation as “*dropout_p02_swap_p02_mix_p02_sparse40_p01_noise10_p01*” and randomly augment 50% source samples during source training.
- **SN**: SN [42] normalizes car sizes on the source domain with statistics of car sizes on the target domain. Given our experimental settings, we also apply it to pedestrians and cyclists.
- **ST3D++ and ROS**: Follow the recommended settings and the released code in [49], we apply the UDA ST3D++ and its ROS augmentation to the unified VoxelRCNN model to detect all objects of interest.
- **Rain**: According to [17], the severity level of rain simulation is determined by the parameter *rainfall rate*. After investigation, we randomly select one *rainfall rate* from the broad range {10, 20, 30, 40, 50}mm/hr to simulate the rain in the point cloud.
- **Fog**: Following the recommended settings in [11], we randomly select one severity parameter α from the range {0, 0.005, 0.01, 0.02, 0.03, 0.06} to simulate the fog in the point cloud.
- **RBRS**: Following the recommended settings in [15], we adopt RBRS to augment source data on different domains, specifically employing random beam upsampling on NuScenes samples and random beam downsampling on Waymo samples.
- **KNN-TTT**: Following [25], during self-supervised training and test-time adaptation, we first utilize farthest point sampling to sample 128 keypoints in the point cloud and cluster all points by KNN. Then we down-sample the points by randomly masking 90% clusters as the settings in [25].

Our proposed method. PDDA in Section 4.1 and density down-sampling operations in Sections 4.2 and 4.3 work the pre-processing data augmentations to diversify the point clouds. In particular, the density down-sampling in test-time adaptation is applied as the test-time augmentation and only original point clouds before the density down-sampling are used in the target domain testing for the fair model evaluation.

Regarding the implementation of the decoder, we utilize the *SparseInverseConv3d* of the Python package *spconv* to conduct 8×up-sampling to restore the point cloud with the original point density, considering the 8×down-sampling by *SparseConv3d* adopted in the encoder module of the VoxelRCNN model.

Table 7. Data augmentation ablations in AP(%) on NuScenes → KITTI. The bold **values** represent the best performance in DG tasks and the underlined values for the best performance in DG + UDA tasks.

Tasks	Methods	Car	Pedestrian	Cyclist	mAP
DG	Source-only	62.69/19.02	22.72/18.37	20.61/18.13	35.34/18.5
	PA-DA	65.09/32.44	18.73/14.94	18.66/15.91	34.16/21.1
	3D-VF	65.36/29.21	24.85/20.87	22.13/19.31	37.45/23.13
	Fog	68.16/29.54	24.55/19.24	24.26/20.25	38.99/23.01
	Rain	66.04/30.58	23.81/19.56	21.26/19.24	37.04/23.12
UDA	PDDA	72.69/31.83	<u>27.1/20.93</u>	23.41/19.48	41.07/24.08
	RBRS	65.86/22.78	23.07/17.01	<u>28.71/22.67</u>	39.21/20.82
	SN	<u>70.5/54.78</u>	19.71/15.42	13.36/10.83	34.52/27.01
ROS	ROS	<u>76.29/53.07</u>	17.41/13.34	20.85/18.46	38.18/ <u>28.29</u>

Table 8. Data augmentation ablations in AP(%) on Waymo → NuScenes. The bold **values** represent the best performance in DG tasks and the underlined values for the best performance in DG + UDA tasks.

Tasks	Methods	Car	Pedestrian	Cyclist	mAP
DG	Source-only	31.20/19.13	10.52/8.39	0.75/0.55	14.16/9.36
	PA-DA	29.43/18.06	10.84/8.43	0.82/0.43	13.70/8.97
	3D-VF	30.17/18.91	10.54/7.23	0.76/0.78	13.82/8.97
	Fog	31.50/19.34	11.65/8.82	0.61/0.14	14.59/9.43
	Rain	32.68/19.55	12.08/9.29	0.87/0.74	15.21/9.86
UDA	PDDA	<u>35.67/22.25</u>	13.79/10.08	<u>1.03/0.79</u>	16.83/11.04
	RBRS	35.04/21.43	<u>16.00/11.50</u>	0.95/0.67	<u>17.33/11.20</u>
	SN	29.32/18.84	12.72/10.57	0.72/0.45	14.25/9.96
ROS	ROS	29.36/17.42	10.76/8.53	0.88/0.62	13.67/8.86

8.2. Ablation Study

Table 6 shows the performance of the test-time adaptation with/without the perceptual loss. It illustrates that while additionally adopting the perceptual loss brings slight improvement during test-time parameter updating, it worsens the computing burden and causes severe computational latency.

Tables 7 and 8 depict the performance of different augmentation methods on the detection of all object classes on NuScenes → KITTI and Waymo → NuScenes, respectively. As shown in Table 7, despite not achieving the best performance on all object classes among DG augmentation methods, our proposed PDDA has the best accuracy averaged on all object classes on NuScenes → KITTI. Table 8 indicates the best performance of PDDA among all DG augmentation methods on the detection of all object classes and even the best performance of PDDA among all DG+UDA augmentation methods on the detection of “Car” and “Cyclist” on Waymo → NuScenes.

Table 9 shows the effect of individual components on detecting all object classes on NuScenes → KITTI. It illustrates the significant improvements of the PDDA augmentation on the detection of all object classes and the further improvement of the test-time adaptation on the detection of

Table 9. Component ablations in AP(%) on NuScenes → KITTI. **Source** represents the conventional training procedure. **PDDA**, **MTL** and **TTA** represent our data augmentation, multi-task learning, and test-time adaptation, respectively. The bold **values** represent the best performance.

	Source	PDDA	MTL	TTA	Car	Pedestrian	Cyclist	mAP
(a)	✓				62.69/19.02	22.72/18.37	20.61/18.13	35.34/18.5
(b)	✓	✓			72.69/31.83	27.1/20.93	23.41/19.48	41.07/24.08
(c)	✓	✓	✓		71.49/30.18	28.53/22.61	24.03/19.57	41.35/24.12
(d)	✓	✓	✓	✓	73.58/33.11	30.01/23.73	22.93/18.62	42.17/25.15

Table 10. Component ablations in AP(%) on Waymo → NuScenes. **Source** represents the conventional training procedure. **PDDA**, **MTL** and **TTA** represent our data augmentation, multi-task learning, and test-time adaptation, respectively. The bold **values** represent the best performance.

	Source	PDDA	MTL	TTA	Car	Pedestrian	Cyclist	mAP
(a)	✓				31.2/19.13	10.52/8.39	0.75/0.55	14.16/9.36
(b)	✓	✓			35.67/22.25	13.79/10.08	1.03/0.79	16.83/11.04
(c)	✓	✓	✓		35.69/22.15	14.46/10.46	1.12/0.89	17.09/11.17
(d)	✓	✓	✓	✓	36.04/22.25	14.48/10.56	1.15/0.95	17.22/11.26

“Car” and “Pedestrian”.

Table 10 shows the effect of individual components on detecting all object classes on Waymo → NuScenes. It illustrates the significant performance improvements of the PDDA augmentation and the further performance improvement of the proposed test-time adaptation on detecting all object classes.